Design and synthesis of concentration gradient Prussian blue analogues.

SuKyung Jeon, Carissa H Li, and Daniel R. Talham*

ABSTRACT: A synthetic route to mixed composition particles based on different Prussian blue analogues containing gradient in either the divalent metal or the hexacyanometallate components is explored. Synthetic conditions and combinations of components that favor kinetically trapping the gradient structures are identified and these are contrasted to cases for which gradients in composition are harder to achieve. By exploring several combinations, the relative rate of precipitation of the PBA components is shown to be the crucial determinant for achieving control over the gradient synthesis, a parameter which is complicated by differing crystallization mechanisms within the PBA family. For one combination, cobalt hexacyanoferrate with nickel hexacyanoferrate, a complete series of particles is demonstrated, including particles with differing divalent metal ion gradients, core particles with a gradient shell, and particles with discrete core and shell components separated by a gradient. The structural characteristics of the gradient heterostructures are compared to the individual single phases and to more standard core-shell particles

INTRODUCTION

Prussian blue, often thought of as the first coordination polymer, and the extended family of mixed-metal Prussian blue analogues (PBAs) have featured in research and applications in areas that include electrochromics[1-3] and photochromics,[4] magnetism and light-switchable magnetism,[5-7] ion storage and batteries,[8-11] and, inspired by Prussian blue itself having approved medical uses, a range of biomedical applications.[12, 13] Much of this work benefits from readily accessible preparation methods and the rather unique ability within the realm of coordination networks to control the size and architecture of particles at the nanoscale and mesoscale. For example, many studies involving PBAs have taken advantage of the additive and synergistic response of mixed-compositions and heterostructures, including core-shell[14-17] particles and some even more complex architectures.[18-23]

Recently, PBA concentration gradient particles were developed and investigated for different applications.[24, 25] Concentration gradients are often encountered in materials chemistry, for example in microelectronics to prepare lattice-matched interfaces or for battery electrode materials to reduce charge build-up at interfaces,[26-28] and similar applications were targeted with PBA gradients.[25] A gradient based on the core-rich copper hexacyanoferrate (CuFe-PBA) and shell-rich nickel hexacyanoferrate (NiFe-PBA) was studied as a battery cathode material.[29] The CuFe-PBA is an attractive target as a battery cathode material because two redox active metals result in high capacities, but the copper analogue is susceptible to a charge-state dependent structural transition that limits cycleability.[17] A core-shell system with a NiFe-PBA shell was shown to suppress the detrimental phase transition[17] while maintaining higher capacity.[17] The gradient system, g-CuNi[Fe(CN)$_6$], copper rich at the core and nickel rich at the surface, also suppressed the phase change and displayed improved rate capability and cycling compared the analogous core-shell, CuFe-PBA@NiFe-PBA, attributed to reducing the detrimental build-up of charge at the interface between the separate components present in core-shell heterostructures.[29] A similar strategy was adopted using a gradient based on manganese hexacyanoferrate and nickel hexacyanoferrate.[25] In another example, a gradient system was developed for study as a multimodal nanotheranostic, combining photothermal properties with MRI contrast enhancement.[24] The particles were based on Prussian blue, which had been previously studied as a photothermal agent[24], combining it with a gadolinium analogue previously shown to act as a positive MRI contrast agent.[24] The T_1 contrast comes principally from interactions at the surface of the particle, so by concentrating Gd^{3+} ions near the surface, the T_1 contrast efficiency, typically measured as the per mole of gadolinium relaxivity, was maximized.

Multiple methods have successfully been applied to manipulate the architecture and size of coordination network particles, particularly PBAs.[30-32] The use of microemulsions[30] was one of the earliest strategies to achieve colloidally stable nanometer scale PBA particles. Polymer and ligand-assisted methods that control the precipitation rate and provide functionalized surfaces to stabilize the particles have also been used, as have hard templates, such as silica or mesoporous silica,[33] chitosan,[34] or alginate beads[35] Syntheses to achieve particles ranging in size from a few nanometers to a micron or larger have been reported. In contrast to the templated and ligand-assisted methods, Catala and co-workers developed a strategy to yield self-stabilized PBA nanoparticles in the absence of surface modifiers.[36, 37] This controlled co-precipitation method yields particles with an anionic

surface charge, leading to colloidal stabilization. The absence of a surface modifier allows the particle surfaces to remain chemically active, which has been exploited to grow overlayers leading to complex heterostructures such as core-shell particles, core-multishell, hollow and hollow core-shell particles[18, 37, 38]. The co-precipitation approach to mixed-metal PBAs has also been used for the preparation of concentration gradient particles.[24, 29]

The present article takes an in-depth look at the practical elements of synthesizing gradient PBA particles. The focus is on understanding when PBA pairs can be expected to form gradients rather than precipitating as separate phases, as well as the experimental factors that control the successful gradient synthesis. As gradients are kinetic products, the preparations depend on the precipitation rates of the individual components, but different particle growth mechanisms[39] within the PBA family are also shown to play a role in the ability to form the gradient structures. The study is extended to more complex architectures, including core-gradient particles and particles with core and shell analogues separated by a gradient.

Prussian blue analogues have general formula $A_jM_k[M'(CN)_6]_l{\cdot}nH_2O$, in which A is normally an alkali metal ion, M is normally a divalent transition metal ion that bridges the hexacyanometallate ions, $[M'(CN)_6]^{3-}$, in the cubic Prussian blue network. The typically non-integer stoichiometry reflects variable extents of cyanometallate vacancies in most examples. For the remainder of the paper, the single phase PBAs will be abbreviated as AMM'-PBA (or simply MM'-PBA if the alkali metal ion is implied). The concentration gradient particles for which the divalent metal ions are varied will be denoted as g-$M_1M_2[M'(CN)_6]$, where M1 and M2 indicate the order in which the divalent metal ion precursors are added during synthesis. Therefore, g-CoNi$[Fe(CN)_6]$ indicates the Co^{2+} precursor is added as the core-rich component and Ni^{2+} as the shell-rich component. Gradients can also be formed by varying the hexacyanometallate during synthesis, such as to form g-Ni$[Fe(CN)_6][Cr(CN)_6]$, where hexacyanoferrate at the core of the particle gradually gives way to hexacyanochromate toward the surface.

▪ EXPERIMENTAL SECTION

Material Preparation. All reagents are purchased from Sigma-Aldrich, Alfa Aesar, and Fischer Certified Reagent and used without further purification. Deionized water used in the synthetic procedures is obtained from a Barnstead NANOpure filtration system.

Series 1. Single-Phase Particles. In a synthesis of single phase CoFe-PBA particles, separate solutions of $CoCl_2 \cdot nH_2O$ (96 mg, 0.4 mmol) and of $K_3[Fe(CN)_6]$ (148 mg, 0.47 mmol) were prepared, each in 100 mL of NANOpure water. The two aqueous solutions were then added dropwise to 200 mL of water at a rate of 2 mL/min using a peristaltic pump under stirring. The resulting suspension was allowed to stir for 18 hours. The particles were collected by centrifugation at 10000 rpm for 10 min and subsequently rinsed with 300 mL of NANOpure water and dried by evaporation at room temperature. Other members of the series were prepared using the same method substituting the appropriate divalent metal chloride.

Sample 1-1. $K_{0.1}Co[Fe(CN)_6]_{0.7}{\cdot}nH_2O$ (CoFe-PBA). Brown powder. IR (KBr) 2122 cm^{-1}($\tilde{\nu}$CN terminal, Co^{II}-NC-Fe^{III}) and 2094 cm^{-1}($\tilde{\nu}$CN terminal, Co^{II}-NC-Fe^{II}) Space group and lattice parameter: Fm-3m and 10.31 Å. Bulk EDS atomic % (Co/Fe): 52.6/38.9.

Sample 1-2. $K_{0.1}Ni[Fe(CN)_6]_{0.7}{\cdot}nH_2O$ (NiFe-PBA). Yellow powder. IR (KBr) 2170 cm-1 ($\tilde{\nu}$CN, Ni^{II}-NC-Fe^{III}), 2125 cm^{-1} ($\tilde{\nu}$CN terminal, Ni^{II}-NC-Fe^{III}) and 2102 cm-1 ($\tilde{\nu}$CN, NiII-NC-FeII), Space group and lattice parameter: Fm-3m and 10.21 Å. Bulk EDS atomic % (Ni/Fe): 50.5/35.4.

Sample 1-3. $K_{0.1}Cu[Fe(CN)_6]_{0.7}{\cdot}nH_2O$ (CuFe-PBA). Light brown powder. IR (KBr) 2108 cm^{-1} ($\tilde{\nu}$CN, Cu^{II}-NC-Fe^{III}), Space group and lattice parameter: Fm-3m and 10.15 Å Bulk EDS atomic % (Cu/Fe): 52.0/36.7.

Series 2. Core@Shell Particles. In a synthesis of the core-shell sample, CoFe-PBA@NiFe-PBA, the previously prepared single-phase CoFe-PBA particles were re-dispersed in 400 mL NANOpure water. A 200 mL aqueous solution of $NiCl_2 \cdot 6H_2O$ (0.4 mmol) and an equal volume of an aqueous solution of $K_3[Fe(CN)_6]$ (148 mg, 0.47 mmol) were added to the core suspension at 10 mL/hr using a peristaltic pump. The particles were collected and isolated by centrifugation, as described above. The stoichiometry of core and shell is determined assuming the core composition maintains the same ratio in the core-shell product.

Sample 2-1. $K_{0.1}Co[Fe(CN)_6]_{0.7}$@$K_{0.1}Ni[Fe(CN)_6]$ nH_2O (CoFe-PBA@NiFe-PBA). Reddish brown powder. IR (KBr): 2164 cm^{-1} ($\tilde{\nu}$CN, $Co^{II}_{(HS)}$-NC-Fe^{III} and Ni^{II}-NC-Fe^{III}), 2122 cm^{-1} ($\tilde{\nu}$CN, $Co^{II}_{(LS)}$-NC-Fe^{III}) and 2100 cm^{-1} ($\tilde{\nu}$CN, Co^{II}-NC-Fe^{II}), Space group and lattice parameter: Fm-3m and 10.23 Å and 10.28 Å. ICP-AES Core (Co/Fe in mg/L): 23.3/15.4. Shell (Co/Ni/Fe in mg/L): 11.5/36.2/33.0.

Series 3. Concentration gradient particles

Series 3A. Concentration gradient particles with equimolar divalent metal ion. In a synthesis of the concentration gradient g-CoNiFe PBA particles, separate solutions of $CoCl_2 \cdot 6H_2O$ and $NiCl_2{\cdot}6H_2O$ (0.2 mmol) were prepared, each in 50 mL of NANOpure water, and twice the volume of an aqueous solution containing $K_3[FeCN)_6]$ (148 mg, 0.47 mmol) was also prepared. During the reaction, the aqueous solution of $NiCl_2{\cdot}6H_2O$ was constantly added at a rate of 1 mL/min to the aqueous solution of $CoCl_2{\cdot}6H_2O$, thus, gradually increasing the nickel ion concentration in the divalent metal ion precursor solution. Concurrently, the Co^{2+}/Ni^{2+} mixture and the $K_3[Fe(CN)_6]$ solution were each added dropwise to 200 mL of NANOpure water at twice the rate of 2 mL/min using a peristaltic pump under stirring. The resulting suspension was allowed to stir for 18 hours. The particles were collected and isolated by centrifugation, as described above. Other members of the series were prepared using the same method substituting the appropriate divalent metal chlorides and potassium hexacyanometallate. The

same synthetic protocol was followed when the syntheses were performed above or below room temperature. Temperatures use for samples prepared at other than room temperature are indicated in the sample abbreviation.

Sample 3-1. g-$K_{0.1}Co_{0.5}Ni_{0.5}[Fe(CN)_6]_{0.7}\cdot nH_2O$ (g-CoNi[Fe(CN)$_6$]). Reddish brown powder. IR (KBr): 2163 cm^{-1} ($\tilde{\nu}$CN, Co^{II}(HS)-NC-Fe^{III} and Ni^{II}-NC-Fe^{III}), 2122 cm^{-1} ($\tilde{\nu}$CN, Co^{II}(LS) -NC-Fe^{III}), and 2100 cm^{-1} ($\tilde{\nu}$CN, Co^{II}-NC-Fe^{II}). Space group and lattice parameter: Fm-3m and 10.26 Å. ICP-AES (Co/Ni/Fe in mg/L): 17.3/16.2/22.6.

Sample 3-2. g-$K_{0.1}Cu_{0.5}Ni_{0.5}[Fe(CN)_6]_{0.7}\cdot nH_2O$ (g-CuNi[Fe(CN)$_6$]). Light brown powder.IR (KBr): 2172 cm-1 ($\tilde{\nu}$CN, NiII-NC-FeIII) and 2103 cm-1 ($\tilde{\nu}$CN, CuII-NC-FeIII) Space group and lattice parameter: Fm-3m and 10.17 Å. ICP-AES (Cu/Ni/Fe in mg/L): 14.2/13.5/18.0.

Sample 3-3. g-$K_{0.1}Ni_{0.5}Cu_{0.5}[Fe(CN)_6]_{0.7}\cdot nH_2O$ (g-NiCu[Fe(CN)$_6$]). Light brown powder. IR (KBr): 2170 cm^{-1} ($\tilde{\nu}$CN, Ni^{II}-NC-Fe^{III}) and 2102 cm^{-1} ($\tilde{\nu}$CN, Cu^{II}-NC-Fe^{III}). Space group and lattice parameter: Fm-3m and 10.18 Å. ICP-AES (Ni/Cu/Fe in mg/L): 31.0/32.4/42.4.

Sample 3-4. g-$K_{0.1}Co_{0.5}Ni_{0.5}[Cr(CN)_6]_{0.7}\cdot nH_2O$ (g-CoNi[Cr(CN)$_6$]): Light pink powder. IR (KBr): 2175 cm^{-1} ($\tilde{\nu}$CN, Co^{II}-NC-Fe^{III} and Co^{II}-NC-Cr^{III}). Space group and lattice parameter: Fm-3m and 10.51 Å. ICP-AES (Co/Ni/Cr in mg/L): 19.4/19.9/24.5.

Sample 3-5. g-$K_{0.1}Ni\{[Cr(CN)_6]_{0.5}[Fe(CN)_6]_{0.5}\}_{0.7}\cdot nH_2O$ (g-Ni[Cr(CN)$_6$][Fe(CN)$_6$]). Light yellow powder. IR (KBr): 2165 cm^{-1} ($\tilde{\nu}$CN, Ni^{II}-NC-Cr^{III} and Ni^{II}-NC-Fe^{III}), 2125 cm^{-1} ($\tilde{\nu}$CN terminal, Ni^{II}-NC-Fe^{III}), and 2100 cm^{-1} ($\tilde{\nu}$CN, Ni^{II}-NC-Fe^{II}). Space group and lattice parameter: Fm-3m and 10.35 Å. ICP-AES (Ni/Cr/Fe in mg/L): 57.4/19.4/17.8.

Sample 3-6. g-$K_{0.1}Co\{[Fe(CN)_6]_{0.7}[Cr(CN)_6]_{0.3}\}_{0.7}\cdot nH_2O$ (g-Co[Fe(CN)$_6$][Cr(CN)$_6$]). Reddish brown powder. IR (KBr): 2157 cm^{-1} ($\tilde{\nu}$CN, Co^{II}-NC-Cr^{III} and Co^{II}-NC-Fe^{III}) and 2089 cm^{-1} ($\tilde{\nu}$CN, Co^{II}-NC-Fe^{II}). Space group and lattice parameter: Fm-3m and 10.32 Å. ICP-AES (Co/Fe/Cr in mg/L): 13.4/6.3/2.6.

Sample 3-7. g-$K_{0.1}Co_{0.5}Ni_{0.5}[Fe(CN)_6]_{0.7}\cdot nH_2O$ at 4°C (g-CoNi[Fe(CN)$_6$] at 4°C). Reddish brown powder. IR (KBr): 2164 cm^{-1} ($\tilde{\nu}$CN, Co^{II}(HS)-NC-Fe^{III} and Ni^{II}-NC-Fe^{III}), 2121 cm^{-1} ($\tilde{\nu}$CN, Co^{II}(LS) -NC-Fe^{III}) and 2095 cm^{-1} ($\tilde{\nu}$CN, Co^{II}-NC-Fe^{II}). Space group and lattice parameter: Fm-3m and 10.26 Å. ICP-AES (Co/Ni/Fe in mg/L): 16.9/17.9/23.8.

Sample 3-8. g-$K_{0.4}Co_{0.5}Ni_{0.5}[Fe(CN)_6]_{0.8}\cdot nH_2O$ at 90°C (g-CoNi[Fe(CN)$_6$] at 90°C). Reddish brown powder. IR (KBr): 2162 cm^{-1} ($\tilde{\nu}$CN, Co^{II}(HS)-NC-Fe^{III} and Ni^{II}-NC-Fe^{III}) and 2094 cm^{-1} ($\tilde{\nu}$CN, Co^{II}-NC-Fe^{II}) Space group and lattice parameter: Fm-3m and 10.26 Å. ICP-AES (Co/Ni/Fe in mg/L): 18.7/18.3/26.5.

Sample 3-9. g-$K_{0.07}Ni_{0.5}Co_{0.5}[Fe(CN)_6]_{0.69}\cdot nH_2O$ at 90°C (g-NiCo[Fe(CN)$_6$] at 90°C). Reddish brown powder. IR (KBr): 2163 cm^{-1} ($\tilde{\nu}$CN, Co^{II}(HS)-NC-Fe^{III} and Ni^{II}-NC-Fe^{III}) and 2122 cm^{-1} ($\tilde{\nu}$CN, Co^{II}(LS) -NC-Fe^{III}), and 2095 cm^{-1} ($\tilde{\nu}$CN, Co^{II}-NC-Fe^{II}). Space group and lattice parameter: Fm-3m and 10.26 Å. ICP-AES (Co/Ni/Fe in mg/L): 8.6/8.5/11.7.

Series 3B. Concentration gradient particles with different divalent metal ratios. In a synthesis of the concentration gradient g-CoNi[Fe(CN)$_6$] particles with a 1:3 Co:Ni ratio, CoCl2·6H2O (0.1 mmol) and NiCl2·6H2O (0.3 mmol) were dissolved separately in 50 mL of NANOpure water and twice the volume of an aqueous solution containing K_3[FeCN)$_6$] (148 mg, 0.47 mmol) was prepared. During the reaction, the aqueous solution of NiCl2·6H2O was added dropwise to the aqueous solution of CoCl2·6H2O, thus, gradually increasing the concentration of transition metal of Ni^{2+} in the precursor solution. Concurrently, the homogeneous Co-Ni mixture and the K_3[Fe(CN)$_6$] solution were added dropwise to 200 mL of NANOpure water at a rate of 2 mL/min using a peristaltic pump under stirring. The resulting suspension was allowed to stir for 18 hours. The particles were collected and isolated by centrifugation, as described above.

Sample 3-10. g-$K_{0.1}Co_{0.25}Ni_{0.75}[Fe(CN)_6]_{0.7}\cdot nH_2O$ (g-CoNi[Fe(CN)$_6$], Co:Ni = 1:3). Reddish brown powder. IR (KBr): 2168 cm^{-1} ($\tilde{\nu}$CN, Co^{II}(HS)-NC-Fe^{III} and Ni^{II}-NC-Fe^{III}) and 2122 cm^{-1} ($\tilde{\nu}$CN, Co^{II}(LS) -NC-Fe^{III}), and 2100 cm^{-1} ($\tilde{\nu}$CN, Co^{II}-NC-Fe^{II}). Space group and lattice parameter: Fm-3m and 10.22 Å. ICP-AES (Co/Ni/Fe in mg/L): 10.6/32.3/28.4.

Series 4. Core@Gradeint Particles. In a synthesis of the core@gradient CoFe@g-CoNi[Fe(CN)$_6$] particles, the previously prepared core CoFe-PBA particles from single phase syntheses were re-dispersed in 400 mL NANOpure water. Separate 100 mL aqueous solutions of $CoCl_2\cdot 6H_2O$ and $NiCl_2\cdot 6H_2O$ (0.38 mmol) were prepared, as well as twice the volume of an aqueous solution of K_3[Fe(CN)$_6$] (276 mg, 0.84 mmol). During the reaction, the aqueous solution of $NiCl_2$ $6H_2O$ was added to the aqueous solution of $CoCl_2$ $6H_2O$ at 8 mL/hr, thus, gradually increasing the concentration Ni^{2+} in the aqueous solution of $CoCl_2\cdot 6H_2O$. Concurrently, the Co-Ni mixture and the K_3[Fe(CN)$_6$] solution were added dropwise to the suspension of core particles at a rate of 15 mL/hr using a peristaltic pump under stirring. The heterostructure core-gradient particles were collected and isolated by centrifugation, as described above. Other members of the series were prepared using the same method substituting the appropriate divalent metal chloride and potassium hexacyanometallate. The stoichiometry of core@gradient is determined assuming the core composition does not change during the synthesis.

Sample 4-1. $K_{0.1}Co[Fe(CN)_6]_{0.7}$@ g-$KCoNi[Fe(CN)_6]_{0.68}\cdot nH_2O$ (CoFe@g-CoNi[Fe(CN)$_6$]). Light yellow brown powder. IR (KBr): 2170 cm^{-1} (vCN, Ni^{II}-NC-Fe^{III}) and 2102 cm^{-1} ($\tilde{\nu}$CN, Cu^{II}-NC-Fe^{III}) Space group and lattice parameter: Fm-3m and 10.35 Å. ICP-AES Core (Co/Fe in mg/L): 25.6/18.1.

Sample 4-2. $K_{0.1}Ni[Fe(CN)_6]_{0.7}$@g-$KNiCu[Fe(CN)_6]\cdot nH_2O$ (NiFe@g-NiCu[Fe(CN)$_6$]). Light yellow brown powder. IR (KBr): 2170 cm^{-1} (vCN, Ni^{II}-NC-Fe^{III}) and 2102 cm^{-1} ($\tilde{\nu}$CN, Cu^{II}-NC-Fe^{III}) Space group and lattice parameter: Fm-3m and 10.35 Å. ICP-AES Core (Ni/Fe in mg/L): 7.2/5.1

Series 5. Solid Solution Particles. In a synthesis of the solid solution $CoNi[Fe(CN)_6]$-PBA, Sample 5-1, separate solutions of $CoCl_2 \cdot 6H_2O$ and $NiCl_2 \cdot 6H_2O$ (0.2 mmol) were prepared, each in 50 mL of NANOpure water, and twice the volume of an aqueous solution containing $K_3[FeCN)_6]$ (148 mg, 0.47 mmol) was also prepared. During the reaction, all three precursors were added dropwise to 200 mL of NANOpure water at a rate of 2 mL/min using a peristaltic pump under stirring. The resulting suspension was allowed to stir for 18 hours. The particles were collected and isolated by centrifugation, as described above.

The remaining solid solution samples (Sample 5-2, 5-3, and 5-4) were outcomes of attempted gradient syntheses that resulted in solid solutions, instead. Samples 5-2 and 5-4 contain equimolar divalent metal ions, and resulted attempting the procedure in Series 3A. Sample 5-3 followed the series 3B gradient synthetic procedure, but with a 3:1 ratio of Co^{2+} to Ni^{2+}.

Sample 5-1. $K_{0.04}Co_{0.5}Ni_{0.5}[Fe(CN)_6]_{0.68} \cdot nH2O$ ($CoNi[Fe(CN)_6]$). Reddish brown powder. IR (KBr): 2163 cm^{-1} ($\tilde{\nu}$CN, Co^{II}(HS)-NC-Fe^{III} and Ni^{II}-NC-Fe^{III}), 2119 cm^{-1} ($\tilde{\nu}$CN, Co^{II}(LS) -NC-Fe^{III}), and 2100 cm^{-1} ($\tilde{\nu}$CN, Co^{II}-NC-Fe^{II}). Space group and lattice parameter: Fm-3m and 10.26 Å. ICP-AES (Co/Ni/Fe in mg/L): 12.4/12.0/15.5.

Sample 5-2. $K_{0.1}Ni_{0.5}Co_{0.5}[Fe(CN)_6]_{0.7} \cdot nH2O$ ($CoNi[Fe(CN)_6]$). Reddish brown powder. IR (KBr): 2165 cm^{-1} ($\tilde{\nu}$CN, Co^{II}(HS)-NC-Fe^{III} and Ni^{II}-NC-Fe^{III}) and 2100 cm^{-1} ($\tilde{\nu}$CN, Co^{II}-NC-Fe^{II}). Space group and lattice parameter: Fm-3m and 10.24 Å. ICP-AES (Co/Ni/Fe in mg/L): 18.2/18.9/24.8.

Sample 5-3. $K_{0.22}Co_{0.75}Ni_{0.25}[Fe(CN)_6]_{0.74} \cdot nH2O$ ($CoNi[Fe(CN)_6]$, Co:Ni = 3:1). Reddish brown powder. IR (KBr): 2162 cm^{-1} ($\tilde{\nu}$CN, Co^{II}(HS)-NC-Fe^{III} and Ni^{II}-NC-Fe^{III}) and 2117 cm^{-1} ($\tilde{\nu}$CN, Co^{II}(LS) -NC-Fe^{III}), and 2095 cm^{-1} ($\tilde{\nu}$CN, Co^{II}-NC-Fe^{II}). Space group and lattice parameter: Fm-3m and 10.28 Å. ICP-AES (Co/Ni/Fe in mg/L): 39.3/13.5/36.8.

Sample 5-4. $K_{0.1}Ni_{0.5}Co_{0.5}[Fe(CN)_6]_{0.7} \cdot nH2O$ at 4°C ($CoNi[Fe(CN)_6]$ at 4°C). Reddish brown powder. IR (KBr): 2164 cm^{-1} (Co^{II}(HS)-NC-Fe^{III} and Ni^{II}-NC-Fe^{III}), 2125 cm^{-1} (vCN, Co^{II}(LS) -NC-Fe^{III}), and 2097 cm^{-1} (vCN, Co^{II}-NC-Fe^{II}). Space group and lattice parameter: Fm-3m and 10.24 Å. ICP-AES (Co/Ni/Fe in mg/L): 8.6/8.7/11.7.

Series 6. Core@Gradient@Shell Particles. In a synthesis of the core@gradient@shell CoFe@g-$Co[Fe(CN)_6]Ni[Co(CN)_6]$@NiCo particles, the previously prepared core CoFe-PBA particles from single phase syntheses were re-dispersed in 400 mL NANOpure water. Separate 100 mL aqueous solutions of $CoCl_2 \cdot 6H_2O$ and $NiCl_2 \cdot 6H_2O$ (0.38 mmol) were prepared, as well as twice the volume of an aqueous solution of $K_3[Fe(CN)_6]$ (276 mg, 0.84 mmol). During the reaction, the aqueous solution of $NiCl_2$ $6H_2O$ was added to the aqueous solution of $CoCl_2 \cdot 6H_2O$ at 8mL/hr, thus, gradually increasing the concentration Ni^{2+} in the aqueous solution of $CoCl_2 \cdot 6H_2O$. Concurrently, the Co-Ni mixture and the $K_3[Fe(CN)_6]$ solution were added dropwise to the suspension of core particles at a rate of 15 mL/hr using a peristaltic pump under stirring. The heterostructure core-gradient particles were collected and isolated by centrifugation, as described above. Other members of the series were prepared using the same method substituting the appropriate divalent metal chloride and potassium hexacyanometallate. The stoichiometry of core and shell is determined assuming the core and core-gradient composition maintains the same ratio in the core-gradient-shell product.

Sample 6-1. $Rb_{0.28}Co[Fe(CN)_6]_{0.76}$@g-$RbCo[Fe(CN)_6]KNi[Co(CN)_6]$@$KNi[Co(CN)_6]_{0.70} \cdot nH2O$ (CoFe@g-$Co[Fe(CN)_6]Ni[Co(CN)_6]$@NiCo. Light brown. IR (KBr): 2184 cm^{-1} ($\tilde{\nu}$CN, Ni^{II}-NC-Co^{III}), 2174 cm^{-1} ($\tilde{\nu}$CN, Co^{II}-NC-Fe^{III}), 2136 cm^{-1} ($\tilde{\nu}$CN, Co^{II}(LS)-NC-Fe^{III}), and 2098 cm^{-1} ($\tilde{\nu}$CN, Co^{II}-NC-Fe^{II}). Space group and lattice parameter: Fm-3m and 10.26 Å. ICP-AES (Co/Ni/Fe in mg/L): 12.4/12.0/15.5.

CHARACTERIZATION. Fourier transform infrared spectroscopy (FTIR) is performed with a Nicolet 6700 Thermo Scientific spectrophotometer. Powder samples are suspended in acetone and sonicated for 10 minutes and dropped onto a pressed KBr pellet to produce a thin film of sample on the surface of the pellet.[40] Total of 16 scans are taken in between 400 cm^{-1} to 4000 cm^{-1}. Transmission electron microscopy (TEM) images are taken using a JEOL-2010F HRTEM at 200kV. Copper TEM grids are used for samples that do not contain the element copper while gold TEM grids are used for samples that do contain copper. TEM samples are prepared by adding dropwise 1 mL of a water solution containing ~ 2 mg of product dispersed by sonication to the corresponding grids and allowing them to dry before viewing under TEM. A minimum of 100 particles are used to quantify the average particle size using Image J imaging software, in which a side length of the cubic particles is measured.[41] Energy dispersive X-ray spectroscopy (EDS) analyses are performed with an Oxford Instrumentation EDS X-ray Microanalysis System which is attached to the HR-TEM microscope. A minimum of three scans of each size population is performed on different regions of the samples and then are averaged to give a relative atomic percentage for each element. EDS linescans are performed to observe the localization of metal ions within a single particle. Inductively coupled plasma atomic emission spectroscopy (ICP-AES) measurements are performed on a Varian VISTA RL simultaneous spectrometer with a CCD detector to determine the concentrations of metallic elements. ICP-AES samples were prepared by suspending ~ 5 mg of product with sodium citrate in 10 mL of NANOpure water. After gentle heating, 1 mL of supersaturated disodium ethylenediaminetetraacetate (EDTA) was added to stabilize the solution. Samples were pumped into the instrument using a peristaltic pump at a rate of 1 mL/min. Four standards (0, 1, 10, 100 ppm) of target metals were measured to provide a calibration curve, which is then used to calculate the chemical stoichiometries of the products. Average molecular formulas were calculated using metal ratios obtained either by bulk EDS or by ICP-AES analysis including potassium ion content to achieve

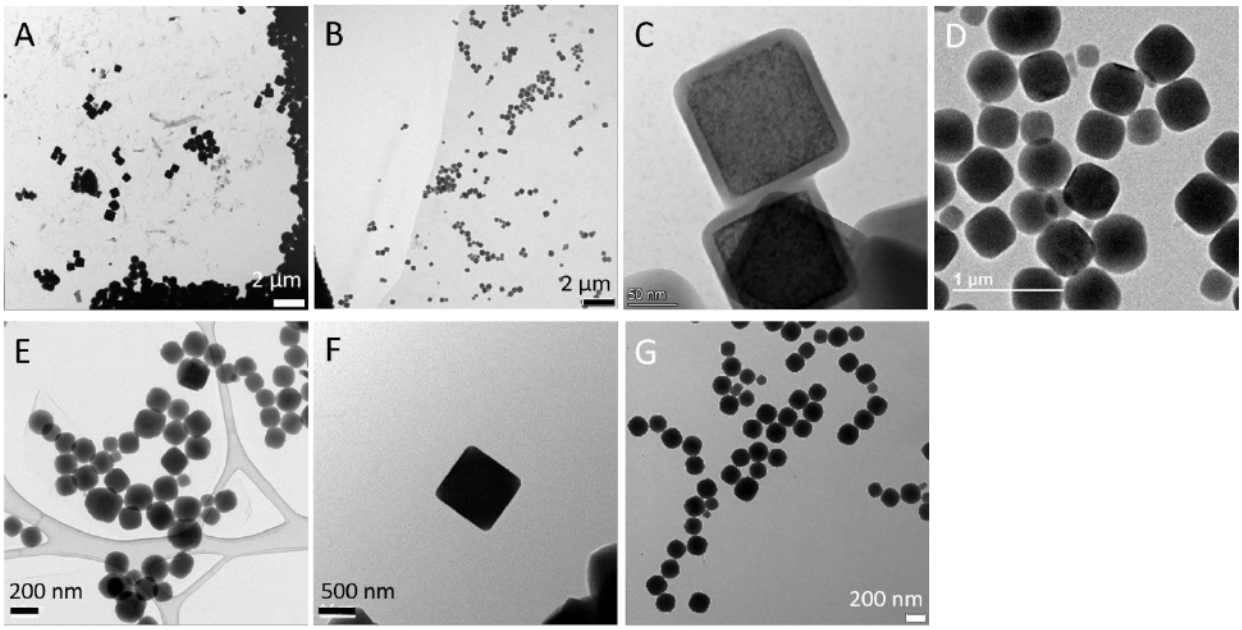

Figure 1. TEM images of samples representing each different particle architectures. A. CoFe-PBA (sample 1-1), B. NiFe-PBA (sample 1-2), C. CoFe-PBA@NiFe-PBA (sample 2-1), D. g-CoNi[Fe(CN)$_6$] (sample 3-1), E. g-NiCo[Fe(CN)$_6$] at 90°C (sample 3-9), F. CoFe@g-CoNi[Fe(CN)$_6$] (sample 4-1), and G. CoNi[Fe(CN)$_6$] (sample 5-1).

	Sample		Average particle size (nm)	Lattice constant (Å)	FWHM (400)
Series 1 (single phase)	1-1	CoFe-PBA	540 ± 80	10.31	0.140 ± 0.003
	1-2	NiFe-PBA	170 ± 30	10.21	0.160 ± 0.002
Series 2 (core-shell)	2-1	CoFe-PBA@NiFe-PBA	160 ± 20	10.28 and 10.23	0.110 ± 0.009 0.170 ± 0.003
Series 3 (concentration gradient)	3-1	g-CoNi[Fe(CN)$_6$]	430 ± 70	10.26	0.170 ± 0.003
Series 4 (core-gradient)	4-1	CoFe@g-CoNi[Fe(CN)$_6$]	780 ± 120	10.26	0.220 ± 0.005
Series 5 (solid solution)	5-1	CoNi[Fe(CN)$_6$]	230 ± 20	10.27	0.150 ± 0.003

Table 1. Particle dimensions, lattice constants and FWHM of (400) reflections for particle samples from the different series 1 to 5. Lattice constants are determined from averaging values based on prominent peaks. The FWHM values are determined by fitting the peak shapes to a Lorentzian function. Data for the remaining samples appear in Supporting Information.

electroneutrality (H_3O^+, while certainly present, is assumed to be a small contributor based on previous studies showing this approach is reliable).[38, 40, 42] While all compositions are known to have both coordinated and interstitial water, precise water content was not measured as it varies significantly with sample handling. In-house measurements of powder X-ray diffraction (PXRD) are taken using an X'Pert powder diffractometer using Cu Ka radiation (λ = 1.5406 Å) with a step size of 0.008° over the 2θ range of 10-60°. Samples are prepared by mounting ~10 mg of particles with a few grains of ground sodium chloride (NaCl) onto a double sided tape on a glass slide. All the XRD patterns are aligned to the NaCl reference peak. In the absence of a suitable lineshape model for the gradient structures, lattice constants were determined by averaging values measured based on prominent peaks.

RESULTS

The concentration gradient PBAs are synthesized with the same coprecipitation method commonly used to prepare nanoscale and mesoscale particles. A typical synthesis begins with dropwise addition of the core-rich divalent metal and the hexacyanometallate into the water. When preparing g-CoNi[Fe(CN)$_6$], the Co^{2+} ion is initially added along with K_3[Fe(CN)$_6$]. At the same time, the solution of the shell-rich metal ion, Ni^{2+} for g-CoNi[Fe(CN)$_6$], is simultaneously added to the core-rich

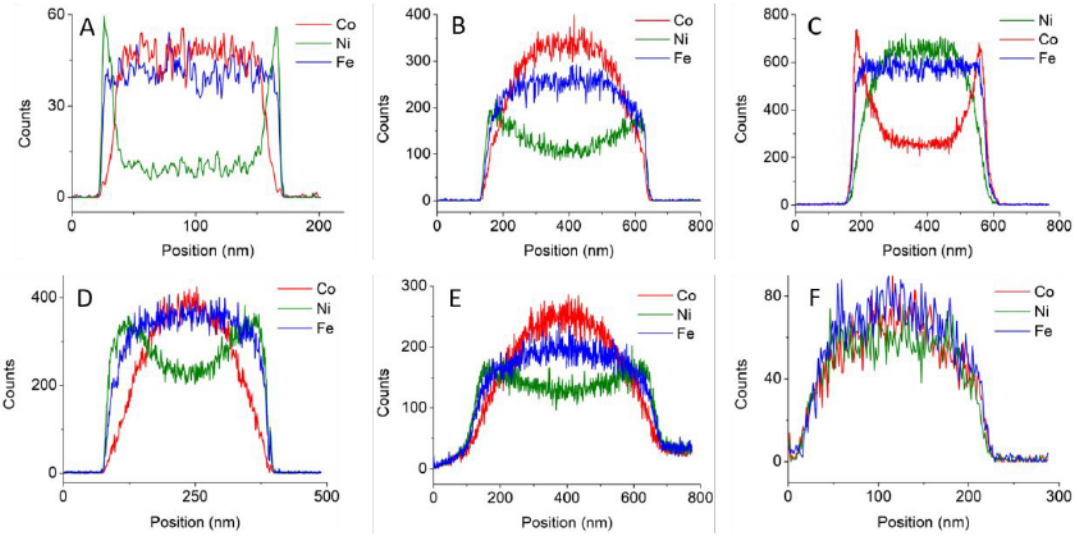

Figure 2. EDS linescans of heterostructure particles. A. CoFe-PBA@NiFe-PBA (sample 2-1), B. g-CoNi[Fe(CN)$_6$] (sample 3-1), C. g-NiCo[Fe(CN)$_6$] at 90°C (sample 3-9), D. g-CoNi[Fe(CN)$_6$] (Co:Ni = 1:3)(sample 3-10), and E. CoFe-PBA@g-CoNi[Fe(CN)$_6$] (sample 4-1), and F. CoNi[Fe(CN)$_6$](sample 5-1). The sample color coding of each metal is included on the plots.

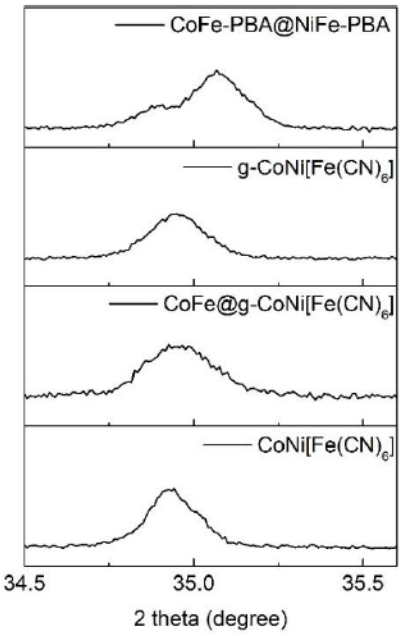

Figure 3. Powder XRD of different structures illustrating the (400) reflection. Full patterns are provided in **Figure S7.**

metal ion solution at half the rate, as indicated in the supporting information, **Scheme S1**, thus gradually changing the ratio of divalent metal ions added to the synthesis. Once the addition is complete, the reaction mixture is stirred overnight and particles are collected by centrifugation. The PBA's are generally poorly soluble, so gradients are achieved when the initial product nucleation is the core-rich PBA with both divalent metal ions incorporated as the particles grow (**Figure S1**). A related architecture, core-gradient particles, are prepared using the same procedures but adding the precursor solutions to a colloidal suspension of uncoated core particles.

Chemical and Structural Analyses of the KCoFe-PBA/KNiFe-PBA Series. Several compositions and particle architectures were explored based on cobalt and nickel hexacyanoferrates in order to contrast the gradient feature with other particle structures. The concentration gradient, g-CoNi[Fe(CN)$_6$], and the core-gradient, CoFe-PBA@g-CoNi[Fe(CN)$_6$], are compared to the core-shell particles, CoFe-PBA@NiFe-PBA, and particles of the single phases CoFe-PBA and NiFe-PBA as well as a solid solution, CoNi[Fe(CN)$_6$].

The morphology and dimensions of these six structures are summarized in **Figure 1** and **Table 1**. The accuracy and reproducibility of the concentration gradient syntheses are further discussed in Table S2 and Figure S2. Each of the preparations yield either cubic particles or cubic particles with rounded edges, with well-defined faces in a 100 – 800 nm size regime. Generally, those with either a shell or a gradient shell were shown to grow into larger particles compared to other structures. In addition, contrast differences seen in TEM images of concentration gradient particles indicate a change in the identity of the PBA species from the core to the surface. Lighter contrast is seen toward the outside of the particles compared to that of a darker core region, reflecting the higher scattering of the CoFe-PBA component[16, 42] (**Figure S3**).

Comprehensive chemical analyses were acquired using EDS, ICP-AES, and FT-IR. The EDS and ICP-AES results support the elemental distribution and stoichiometries anticipated by the fabrication sequence. Vibrational frequencies additionally support the identity of the metal ions and confirm within an uncertainty of a few

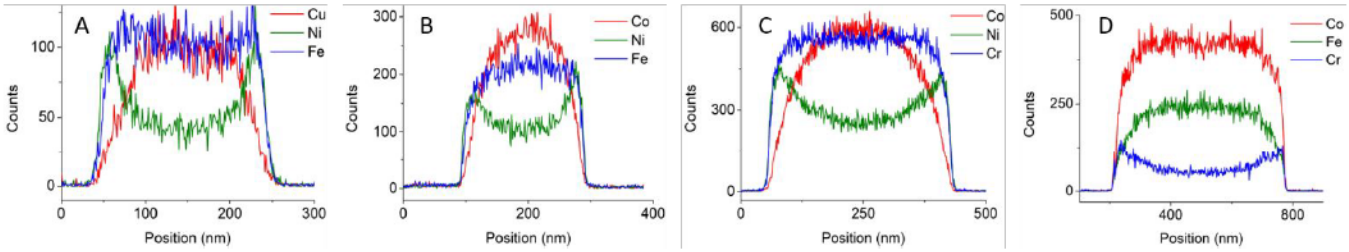

Figure 4. EDS linescans indicating successful gradient syntheses. A. g-CuNi[Fe(CN)$_6$] (sample 3-2), (B) g-CoNi[Fe(CN)$_6$] at 4°C (sample 3-7), C. g-CoNi[Cr(CN)$_6$] (sample 3-4), and D. g-Co[Fe(CN)$_6$][Cr(CN)$_6$] (sample 3-6). The sample color coding of each metal is included on the plots.

percent the oxidation state of the metals in the targeted compounds.[40] Data on chemical compositions and FT-IR frequencies are provided in the Experimental Section. EDS linescans of the mixed-composition samples are shown in **Figure 2**, comparing the elemental profile of the concentration gradient particles to the other architectures. As expected, EDS linescans for g-CoNi[Fe(CN)$_6$] show the Co signal continuously becomes more intense starting from the edge and moving toward the center, whereas a reverse trend is observed for the Ni signal. The EDS profile is dramatically different from the solid solution particle, which shows similar profiles for all elements, or from the core-shell particle with its clear phase segregation between the core and the shell characterized by a sharp discontinuity in the divalent metal profiles at the interface.

The core-gradient structure, CoFe-PBA@g-CoNi[Fe(CN)$_6$], is also shown and appears similar to the simple gradient particle because of the relatively small size of the seed core particle. In general, EDS linescans effectively discern the different mixed-composition architectures.

Structural changes associated with different architectures were investigated using PXRD. The Bragg reflections can be indexed to a face-centered cubic structure with space group Fm-3m. Whereas the separate components are observable for the core-shell particles, the g-CoNi[Fe(CN)$_6$] systems show a single set of peaks with lattice constants that reflect the ratio of constituents, in accordance with Vegard's law,[43] **Table 1 and Figure 3**. The two PBA components, CoFe-PBA and NiFe-PBA, that make up g-CoNi[Fe(CN)$_6$] have lattice constants of 10.31 Å and 10.21 Å. However, as the Co^{2+}: Ni^{2+} ratio is varied from 1:3 to 1:1 when forming gradients, the lattice parameters are reflected accordingly from 10.26 Å for the 1:1 ratio to 10.22 Å for the 1:3 ratio. The diffraction peak widths also reflect the different particle architectures. In **Figure 3**, the (400) reflection of the core-shell particles, CoFe-PBA@NiFe-PBA, are compared to the gradient g-CoNi[Fe(CN)$_6$], the core-gradient CoFe-PBA@g-CoNi[Fe(CN)$_6$], and the solid solution CoNi[Fe(CN)$_6$], with the full width at half maximum (FWHM) for each recorded in **Table 1**. The solid solution particles have peak profiles similar to the single phase particles. Despite the mixed components of the solid-solution, the elemental homogeneity is reflected in the narrower peaks. On the other hand, the gradient and core@gradient systems have broader linewidths, reflecting the varying composition within individual particles.

Chemical and Structural Analyses of the Remaining Series. The EDS linescans of other successful gradient structures are shown in **Figure 4**. Among other examples are g-CoNi[Fe(CN)$_6$ particles formed under different conditions, including a low-temperature synthesis and a gradient with a 1:3 Co^{2+}: Ni^{2+} ratio (**Figure 2**). The core-rich Ni^{2+} gradient, g-NiCo[Fe(CN)$_6$], which was formed at 90 °C is shown, as well as the copper/nickel gradient, g-CuNi[Fe(CN)$_6$]. A gradient hexacyanochromate PBA, g-CoNi[Cr(CN)$_6$], is characterized, along with a gradient in which the hexacyanometallate is varied from core-rich hexacyanoferrate to shell-rich hexacyanochromate, g-Co[Fe(CN)$_6$][Cr(CN)$_6$]. Details of the particle analyses are tabulated in the Supporting Information **Table S1**. In addition, chemical and structural analyses of another novel heterostructure of core-gradient-shell, in which the core and the shell is separated by a composition gradient are presented in Figure S8.

Particle Sizes. Particle sizes for each sample are summarized in Table 1 or Table S1. Despite identical synthetic protocols, there is significant variability in particle sizes as the chemical systems change. Generally, the size of the concentration gradient particles correlates with the size of the single phase core-rich analogue when prepared using the same methods. For example, the g-CoNi[Fe(CN)$_6$] particles with average size 430 + 70 nm more closely resemble the single phase CoFe-PBA with average particle sizes of 550 $\pm$ 80 nm when prepared under the same conditions, than the single phase NiFe-PBA (170 $\pm$ 30 nm). A similar trend is observed when varying the divalent metal ratios. Within the g-CoNi[Fe(CN)$_6$] system, changing the cobalt to nickel ratio from 3:1 to 1:3, results in a steady decrease in average size from 480 $\pm$ 50 nm to 250 $\pm$ 90 nm.

DISCUSSION

Achieving Metastable Kinetic Gradient Architectures. The gradient particles are kinetic products,[44] achieved here by gradually changing the concentrations of the two PBA precursors to yield particles where the identity of metals change from the center to the surface. The metastable architecture is helped by similar

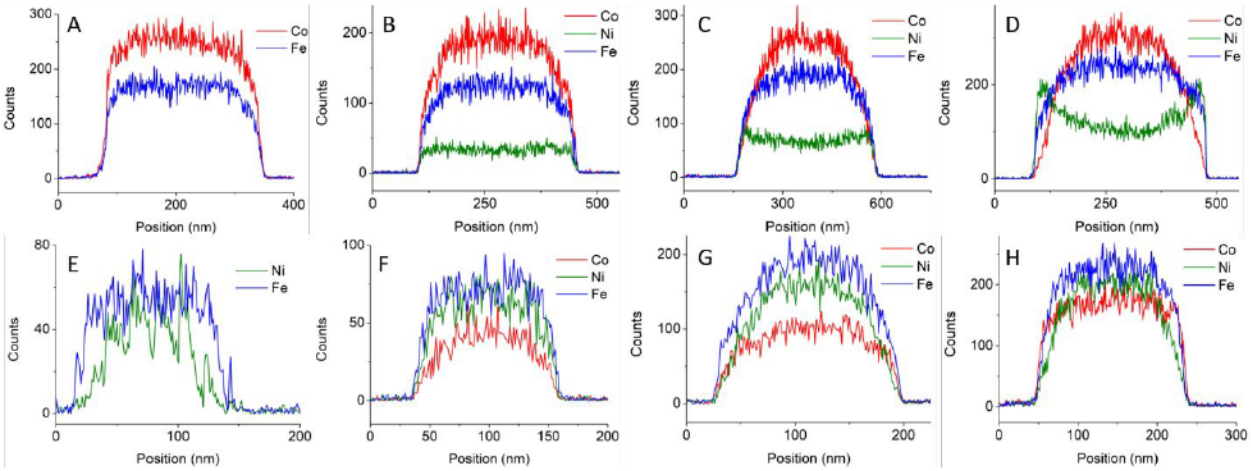

Figure 5. EDS linescans monitoring the metal incorporation of (A-D) g-CoNi[Fe(CN)$_6$] (sample 3-1) and (E-H) g-NiCo[Fe(CN)$_6$] (sample 5-2) particles as a function of addition time under the same gradient synthesis protocol. (A,E) 5 min (B,F) 15 min (C,G) 30 min and (D,H) 50 min. (A-D) displays the gradient metal distribution and (E-H) displays the solid solution metal distribution. The sample color coding of each metal is included on the plots.

lattice parameters and electronic structures of the constituents, and is realized when the product is effectively quenched so phase separation or product annealing is limited. These conditions are met during the room-temperature coprecipitation synthesis of many PBA's due to rapid bond formation and low solubility of the product network solids. **Figure S1** shows how the total ion content of particles harvested during the course of the gradient synthesis of g- CoNi[Fe(CN)$_6$] match the ratios of the precursors added up to the point of each sampling. For several combinations of PBA's, the gradient combinations are easily achieved. In addition to g-CoNi[Fe(CN)$_6$], other examples shown in **Figures 2 and 4** include g-CuNi[Fe(CN)$_6$] and g-CoNi[Cr(CN)$_6$], for which the divalent metal ion occupancy changes from core to shell, and g-Co[Fe(CN)$_6$][Cr(CN)$_6$], for which the hexacyanometallate is varied. On the other hand, for some gradient combinations, like g-NiCu[Fe(CN)$_6$], and g-NiCo[Fe(CN)$_6$], the room temperature synthesis is unsuccessful, yielding separate phases or solid solutions. While the g-NiCo[Fe(CN)$_6$] can be achieved using higher reaction temperature, **Figure 2**, synthesis of the g-NiCu[Fe(CN)$_6$] was not successful at any temperatures. A number of different strategies were pursued in an attempt to obtain a successful g-NiCu[Fe(CN)$_6$] system, provided in Figure S9. The different behavior can be understood when considering differences in reaction rates and crystallization mechanisms within the PBA family.

Systems that Follow the Synthetic Design. A general observation is the co-precipitation route to gradients works well when the precipitation rates of the different components are similar, or if the precipitation rate of the core-rich component is faster. The effects are seen when comparing g-CuNi[Fe(CN)$_6$] with g-NiCu[Fe(CN)$_6$] or comparing g-CoNi[Fe(CN)$_6$] with g-NiCo[Fe(CN)$_6$], pairs for which the core-rich and shell-rich components are reversed. For the copper/nickel series, the gradient co-precipitation works well for g-CuNi[Fe(CN)$_6$], but reversing the order is not successful. A similar result is seen for the cobalt/nickel series at room temperature where the g-CoNi[Fe(CN)$_6$] forms successfully but difficulties arise when trying to prepare a nickel-rich core. Of the single phase components, copper hexacyanoferrate precipitates much faster than the nickel analogue, reflecting the relative water exchange rates for the divalent metal ion precursors.[45] The cobalt hexacyanoferrate precipitation rate at room temperature is intermediate, but also faster than the nickel analogue, as seen in Tyndall effect experiments (**Table S3**) or by monitoring ionic conductivity.[39]

The consequence of the different precipitation rates can be seen by monitoring the composition of particles as they grow during the course of the precursor addition, as shown in **Figure 5** for the cobalt/nickel gradients. For g-CoNi[Fe(CN)$_6$], a CoFe-PBA core forms initially to which Ni^{2+} adds in successively greater amounts to form the Co^{2+}/Ni^{2+} gradient. In fact, in this case, the g-CoNi[Fe(CN)$_6$] particle might be better characterized as a core-gradient particle, reflecting the initial precipitation of the CoFe-PBA. On the other hand, the g-NiCo[Fe(CN)$_6$] synthesis shows a solid solution at nearly all stages of growth, and the incorporation of Ni^{2+} into the particle does not reflect the relative concentrations of precursors, especially at early stages of the reaction.

Although the co-precipitation synthesis of g-NiCo[Fe(CN)$_6$] was not successful at room temperature, a gradient between a nickel-rich core and cobalt-rich shell was realized when performing the reaction at higher temperature. The influence of reaction temperature is displayed in **Figure 6** using EDS linescans to characterize products for both directions of the Co^{2+}/Ni^{2+} gradient. At lower temperature, 4°C, the results are similar to those obtained at room temperature. The gradient with core-rich Co^{2+} and shell-rich Ni^{2+} is achieved, but the reverse results in a solid solution. The effects of more rapid CoFe-

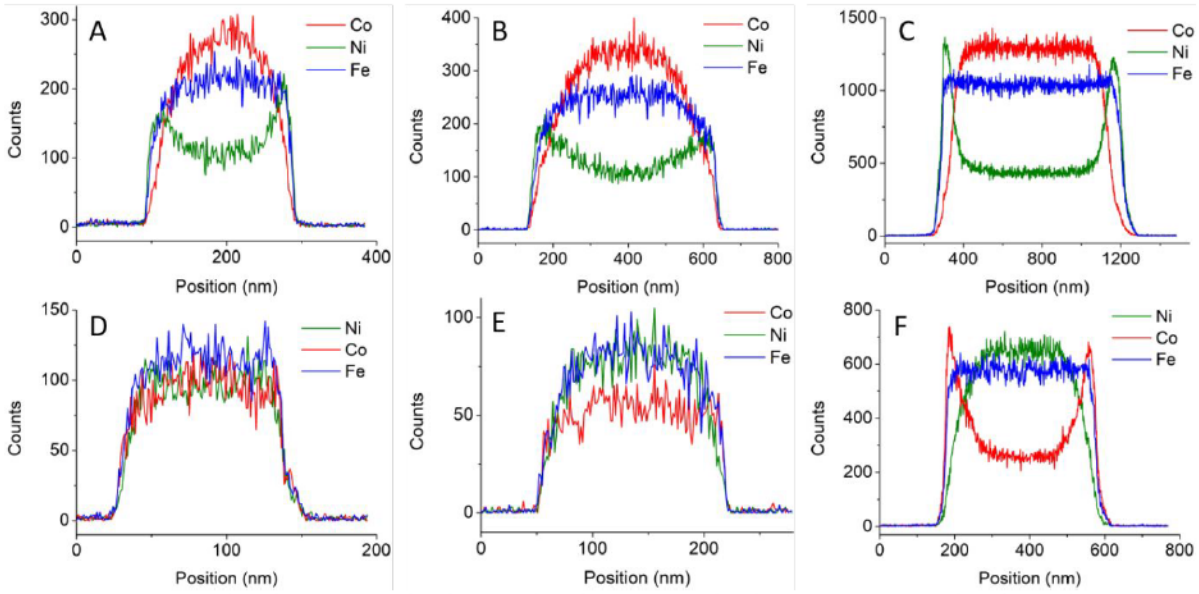

Figure 6. EDS linescans of (A-C) g-CoNi[Fe(CN)$_6$] and (D-E) g-NiCo[Fe(CN)$_6$] synthesized at (A,D) 4°C (sample 3-7 and 5-4), and (B,E) room temperature (sample 3-1 and 5-2) (C,F) 90°C (sample 3-8 and 3-9) following the gradient synthesis protocol. The sample color coding of each metal is included on the plots.

Figure 7. EDS linescan displaying the gradient evolution of g-NiCo[Fe(CN)$_6$] (sample 3-9) synthesized at 90°C as a function of addition time. (A) 15 min (B) 30 min and (C) 50 min

PBA precipitation seen at room temperature also influences the 4 °C behavior. In contrast, at 90 °C, the gradient with Ni^{2+}-rich core to Co^{2+}-rich shell is successful and the different behavior is observable when monitoring particles duringthe course of the reaction. After 15 minutes of reaction, the Ni^{2+}: Co^{2+} ratio added to the reaction is 70:30, and this ratio is reflected in the mole fraction within the particles (**Figure 7**). At higher temperature the Ni^{2+} and Co^{2+} reactivities which show a change in the relative precipitation rates of the two components as the temperature is raised (**Table S3**). At room temperature, the CoFe-PBA precipitates much more quickly than the NiFe-PBA single phase analogue. At 90°C, the CoFe-PBA precipitation time remains about the same as at room temperature, but the NiFe-PBA precipitation becomes much faster, allowing the Ni^{2+} to compete with Co^{2+} during the co-precipitation.

On the other hand, for the Cu^{2+}/Ni^{2+} system, the g-NiCu[Fe(CN)$_6$] was not successful at any temperature and it is interesting to consider why elevated temperature facilitates the gradient formation for g-NiCo[Fe(CN)$_6$] but does not help to form the g-NiCu[Fe(CN)$_6$]. As mentioned above, the aqueous Ni^{2+} ligand exchange rates are slow relative to Cu^{2+} and Co^{2+}. At elevated temperature the exchange rates increase, leading to faster precipitation of the NiFe-PBA. However, the rate is still slow relative to the CuFe-PBA precipitation, as the aqueous Cu^{2+} exchange also increases with temperature. The anomaly is the CoFe-PBA analogue. Even though the aqueous Co^{2+} exchange rate should also increase, the speed of network formation is not significantly affected. The different behavior is likely due to differences in crystallization mechanisms. A recent study by Liang et al[39]. showed that the crystallization of CoFe-PBA particles proceeds via the initial formation of nanometer-scale amorphous precursor objects that subsequently aggregate to form particles of the network solid. Therefore, the CoFe-PBA linkages form via a two-step process, Co^{2+} ligand exchange leading to amorphous precursors, and inclusion of the amorphous aggregates into the growing network solid crystal. The temperature dependence of the two steps is evidently not the same, as faster ligand exchange does not lead to significantly faster particle precipitation. In contrast, the Liang et al[39]. study showed NiFe-PBA particles form via a classical nucleation and growth mechanism, without amorphous precursors. Therefore, when the NiFe-PBA precipitation rate increases

at higher temperature, it can compete with the CoFe-PBA components as the network solid forms. The copper analogue, CuFe-PBA, was also shown to follow a classical crystal nucleation and growth mechanism. Therefore, for the Cu^{2+}/Ni^{2+} gradients, g-CuNi[$Fe(CN)_6$] and g-NiCu[$Fe(CN)_6$], changing temperature should have a similar effect on both components, so the CuFe-PBA component is always much faster, making it easy to form the Cu^{2+} core-rich gradient particles via co-precipitation but problematic for the reverse, Ni^{2+} core-rich particles.

Gradients Combining Two Hexacyanometallates. Other gradient systems prepared using the same synthetic conditions are with two different hexacyanometallates to form g-Ni[$Cr(CN)_6$][$Fe(CN)_6$] and g-Co[$Fe(CN)_6$][$Cr(CN)_6$]. Here, the gradient is achieved by continuously changing the occupancy of hexacyanoferrate and hexacyanochromate. The first example, g-Ni[$Cr(CN)_6$][$Fe(CN)_6$], is comprised of core-rich Cr^{3+} and shell-rich Fe^{3+}. As intended by the synthetic design, the EDS linescans (**Figure 4**) depicted the expected metal-ion distribution. Contrary to the gradients changing the divalent metal ion, this system is expected to have the similar water exchange rates as it is the Lewis base hexacyanmetallate that is changing, not the Lewis acid divalent metal ion. Therefore, the substitution of water molecules by hexacyanometallates can occur according to the order in which the precursors are added. In addition to the EDS linescan, XRD and ICP-AES support the gradient assignment.

The second example is the $[Fe(CN)_6]^{3-}$/ $[Cr(CN)_6]^{3-}$ gradient with Co^{2+} instead of Ni^{2+} to form g-Co[$Fe(CN)_6$][$Cr(CN)_6$]. The EDS linescan of the product suggests hexacyanoferrate is abundant at the center of the particles and the hexacyanochromate is gradually incorporated approaching the surface (**Figure 4**). Interestingly, the Fe:Cr ratio is significantly greater than the 1:1 ratio used in the synthesis. The stoichiometry determined by ICP-AES is consistent with the EDS observation, yielding a 7:3 ratio (**Figure 4**) between the two elements. This result is further reflected in the diffraction patterns (**Figure 10**), for which there is a single pattern corresponding to a lattice parameter of 10.33 Å, following Vegard's law reflecting a higher concentration of CoFe PBA. The unequal hexacyanometallate ratio, appears to be related to the relatively high solubility of the hexacyanochromate product, reducing its incorporation. The unusual behavior of $[Cr(CN)_6]^{3-}$ with some Lewis acids has been noted previously, where linkage isomerism, perhaps facilitated by redox processes, leads to enhanced lability of the hexacyanochromate ions.[46]

CONCLUSION

Mixed composition Prussian blue analogue particles with controlled concentration gradients have been prepared, and the synthetic conditions and component characteristics that lead to uniform gradients have been elucidated. The successful quenching of the kinetic gradient products primarily depends on the relative precipitation rates of the individual PBA species. Comparable precipitation rates allow the facile synthesis of composition gradients using standard coprecipitation syntheses. If the component solubilities differ, gradients can be formed when the analogue with faster formation kinetics makes up the core-rich component. The ability to find synthetic conditions to alter the relative precipitation kinetics of the PBA components, and thereby better control the ability to form a targeted gradient, depends on the crystallization mechanism, which differs within the family of Prussian blue analogues. Using these guidelines, particles with uniform gradients from the core to the surface changing either the divalent metal ion or replacing the cyanometallate have been demonstrated. The synthetic approaches can also be used to prepare more complex heterostructures that incorporate gradient segments, including core-gradient-shell particles and core-shell particles separated by a gradient. The study can lend insight to other studies that could benefit from including composition gradients in nanoscale or mesoscale coordination polymer architectures.

ASSOCIATED CONTENT

Supporting Information.
The Supporting Information is available free of charge at

TEM images and size distribution for all samples; Table of lattice constant and particle dimension of all the synthesized samples and PXRD pattern of each heterostructure

AUTHOR INFORMATION

Corresponding Author

Daniel R. Talham – *Department of Chemistry, University of Florida, Gainesville, Florida 32611-7200, United States*;
Email: talham@chem.ufl.edu

Authors

SuKyung Jeon – *Department of Chemistry, University of Florida, Gainesville, Florida 32611-7200, United States*
Carissa H. Li - *Department of Chemistry, University of Florida, Gainesville, Florida 32611-7200, United States*

ACKNOWLEDGMENT

We acknowledge the financial support by the National Science Foundation Division of Materials Research through award(s) DMR-1904596.

REFERENCES

(1) Itaya, K.; Uchida, I.; Neff, V., Electrochemistry Of Polynuclear Transition-Metal Cyanides-Prussian Blue And Its Analogs. *Acc. Chem. Res.* **1986,** 19, 162-168.

(2) Hedley, L.; Robertson, N.; Johansson, J., Electrochromic Thin Films of the V-Cr Prussian Blue Analogue Molecular Magnet. *Electrochim. Acta* **2017,** 236, 97-103.

(3) Hedley, L.; Porteous, L.; Hutson, D.; Robertson, N.; Johansson, J., Electrochromic bilayers of Prussian blue and its Cr analogue. *J. Mater. Chem. C* **2018,** 6, 512-517.

(4) Nishizawa, M.; Kuwabata, S.; Yoneyama, H., Photoimage formation in a TiO_2 particle-incorporated prussian blue film. *J. Electrochem. Soc.* **1996,** 143, 3462-3465.

(5) Sato, O.; Einaga, Y.; Fujishima, A.; Hashimoto, K., Photoinduced long-range magnetic ordering of a cobalt-iron cyanide. *Inorg. Chem* **1999,** 38, 4405-4412.

(6) Shimamoto, N.; Ohkoshi, S.; Sato, O.; Hashimoto, K., Control of charge-transfer-induced spin transition temperature on cobalt-iron Prussian blue analogues. *Inorg. Chem* **2002,** 41, 678-684.

(7) Tokoro, H.; Matsuda, T.; Nuida, T.; Moritomo, Y.; Ohoyama, K.; Dangui, E.; Boukheddaden, K.; Ohkoshi, S., Visible-light-induced reversible photomagnetism in rubidium manganese hexacyanoferrate. *Chem. Mater.* **2008,** 20, 423-428.

(8) Wessells, C.; McDowell, M.; Peddada, S.; Pasta, M.; Huggins, R.; Cui, Y., Tunable Reaction Potentials in Open Framework Nanoparticle Battery Electrodes for Grid-Scale Energy Storage. *ACS Nano* **2012,** 6, 1688-1694.

(9) Fu, H.; Liu, C.; Zhang, C.; Ma, W.; Wang, K.; Li, Z.; Lu, X.; Cao, G., Enhanced storage of sodium ions in Prussian blue cathode material through nickel doping. *J. Mater. Chem. A* **2017,** 5, 9604-9610.

(10) Li, C.; Nanba, Y.; Asakura, D.; Okubo, M.; Talham, D., Li-ion and Na-ion insertion into size-controlled nickel hexacyanoferrate nanoparticles. *RSC Adv.* **2014,** 4, 24955-24961.

(11) Lu, Y.; Wang, L.; Cheng, J.; Goodenough, J., Prussian blue: a new framework of electrode materials for sodium batteries. *ChemComm* **2012,** 48, 6544-6546.

(12) Mukherjee, S.; Rao, B.; Sreedhar, B.; Paik, P.; Patra, C., Copper Prussian blue analogue: investigation into multifunctional activities for biomedical applications. *ChemComm* **2015,** 51, 7325-7328.

(13) Long, J.; Guari, Y.; Guerin, C.; Larionova, J., Prussian blue type nanoparticles for biomedical applications. *Dalton Trans.* **2016,** 45, 17581-17587.

(14) Okubo, M.; Li, C.; Talham, D., High rate sodium ion insertion into core-shell nanoparticles of Prussian blue analogues. *ChemComm* **2014,** 50, 1353-1355.

(15) Li, C.; Peprah, M.; Asakura, D.; Meisel, M.; Okubo, M.; Talham, D., Stepwise Reduction of Electrochemically Lithiated Core-Shell Heterostructures Based on the Prussian Blue Analogue Coordination Polymers $K_{0.1}Cu[Fe(CN)_6]_{0.7}\cdot 3.5H_2O$ and $K_{0.1}Ni[Fe(CN)_6]_{0.7}\cdot 4.4H_2O$. *Chem. Mater.* **2015,** 27, 1524-1530.

(16) Dumont, M.; Knowles, E.; Guiet, A.; Pajerowski, D.; Gomez, A.; Kycia, S.; Meisel, M.; Talham, D., Photoinduced Magnetism in Core/Shell Prussian Blue Analogue Heterostructures of $K_jNi_k[Cr(CN)_6]_l\cdot nH_2O$ with $Rb_aCo_b[Fe(CN)_6]_c\cdot mH_2O$. *Inorg. Chem.* **2011,** 50, 4295-4300.

(17) Asakura, D.; Li, C.; Mizuno, Y.; Okubo, M.; Zhou, H.; Talham, D., Bimetallic Cyanide-Bridged Coordination Polymers as Lithium Ion Cathode Materials: Core@Shell Nanoparticles with Enhanced Cyclability. *J. Am. Chem. Soc.* **2013,** 135, 2793-2799.

(18) Risset, O.; Knowles, E.; Ma, S.; Meisel, M.; Talham, D., $Rb_jM_k[Fe(CN)_6]_l$ (M = Co, Ni) Prussian Blue Analogue Hollow Nanocubes: a New Example of a Multilevel Pore System. *Chem. Mater.* **2013,** 25, 42-47.

(19) Catala, L.; Mallah, T., Nanoparticles of Prussian blue analogs and related coordination polymers: From information storage to biomedical applications. *Coord. Chem. Rev.* **2017,** 346, 32-61.

(20) Presle, M.; Lemainque, J.; Guigner, J.; Larquet, E.; Maurin, I.; Boilot, J.; Gacoin, T., Controlled growth of core@shell heterostructures based on Prussian blue analogues. *New J. Chem.* **2011,** 35, 1296-1301.

(21) Felix, G.; Nicolazzi, W.; Salmon, L.; Molnar, G.; Perrier, M.; Maurin, G.; Larionova, J.; Long, J.; Guari, Y.; Bousseksou, A., Enhanced Cooperative Interactions at the Nanoscale in Spin-Crossover Materials with a First-Order Phase Transition. *Phys. Rev. Lett.* **2013,** 110, 235701-1- 235701-5.

(22) Folch, B.; Larionova, J.; Guari, Y.; Molvinger, K.; Luna, C.; Sangregorio, C.; Innocenti, C.; Caneschi, A.; Guerin, C., Synthesis and studies of water-soluble Prussian Blue-type nanoparticles into chitosan beads. *Phys. Chem. Chem. Phys.* **2010,** 12, 12760-12770.

(23) Larionova, J.; Guari, Y.; Sangregorio, C.; Guerina, C., Cyano-bridged coordination polymer nanoparticles. *New J. Chem.* **2009,** 33, 1177-1190.

(24) Li, Y.; Li, C.; Talham, D., One-step synthesis of gradient gadolinium ironhexacyanoferrate nanoparticles: a new particle design easily combining MRI contrast and photothermal therapy. *Nanoscale* **2015,** 7, 5209-5216.

(25) Hu, P.; Peng, W.; Wang, B.; Xiao, D.; Ahuja, U.; Rethore, J.; Aifantis, K., Concentration-Gradient Prussian Blue Cathodes for Na-Ion Batteries. *ACS Energy Lett.* **2020,** 5, 100-108.

(26) Sun, Y.; Myung, S.; Park, B.; Prakash, J.; Belharouak, I.; Amine, K., High-energy cathode material for long-life and safe lithium batteries. *Nat. Mater.* **2009,** 8, 320-324.

(27) Song, D.; Hou, P.; Wang, X.; Shi, X.; Zhang, L., Understanding the Origin of Enhanced Performances in Core-Shell and Concentration-Gradient Layered Oxide Cathode Materials. *ACS Appl. Mater. Interfaces* **2015,** 7, 12864-12872.

(28) Hou, P.; Zhang, H.; Zi, Z.; Zhang, L.; Xu, X., Core-shell and concentration-gradient cathodes prepared via co-precipitation reaction for advanced lithium-ion batteries. *J. Mater. Chem. A* **2017,** 5, 4254-4279.

(29) Li, C. Cyanide-bridged coordination polymers as battery cathodes. Ph.D. thesis. University of Florida, Gainesville, FL, 2014.

(30) Moulik, S.; De, G.; Panda, A.; Bhowmik, B.; Das, A., Dispersed molecular aggregates. 1. Synthesis and characterization of nanoparticles of $Cu_2[Fe(CN)_6]$ in H_2O/AOT/*n*-heptane water-in-oil microemulsion media. *Langmuir* **1999,** 15, 8361-8367.

(31) Catala, L.; Gacoin, T.; Boilot, J.; Riviere, E.; Paulsen, C.; Lhotel, E.; Mallah, T., Cyanide-bridged Cr^{III}-Ni^{II} superparamagnetic nanoparticles. *Adv. Mater.* **2003,** 15, 826-829.

(32) Vaucher, S.; Li, M.; Mann, S., Synthesis of Prussian blue nanoparticles and nanocrystal superlattices in reverse microemulsions. *Angew. Chem., Int. Ed.* **2000,** 39, 1793-1796.

(33) Fornasieri, G.; Aouadi, M.; Durand, P.; Beaunier, P.; Riviere, E.; Bleuzen, A., Fully controlled precipitation of photomagnetic CoFe Prussian blue analogue nanoparticles within the ordered mesoporosity of silica monoliths. *Chem. Commun.* **2010,** 46, 8061-8063.

(34) Guari, Y.; Larionova, J.; Molvinger, K.; Folch, B.; Guerin, C., Magnetic water-soluble cyano-bridged metal coordination nano-polymers. *Chem. Commun.* **2006**, 2613-2615.

(35) Tokarev, A.; Agulhon, P.; Long, J.; Quignard, F.; Robitzer, M.; Ferreira, R.; Carlos, L.; Larionova, J.; Guerin, C.; Guari, Y., Synthesis and study of Prussian blue type nanoparticles in an alginate matrix. *J. Mater. Chem.* **2012,** 22, 20232-20242.

(36) Brinzei, D.; Catala, L.; Louvain, N.; Rogez, G.; Stephan, O.; Gloter, A.; Mallah, T., Spontaneous stabilization and isolation of dispersible bimetallic coordination nanoparticles of $Cs_xNi[Cr(CN)_6]_y$. *J. Mater. Chem.* **2006,** 16, 2593-2599.

(37) Catala, L.; Brinzei, D.; Prado, Y.; Gloter, A.; Stephan, O.; Rogez, G.; Mallah, T., Core-Multishell Magnetic Coordination Nanoparticles: Toward Multifunctionality on the Nanoscale. *Angew. Chem., Int. Ed.* **2009,** 48, 183-187.

(38) Risset, O. Coordination polymer structures: Design and photomagnetic properties. Ph.D. Thesis. University of Florida, Gainesville, FL, 2014.

(39) Liang, J.; Li, C.; Talham, D., Growth Mechanisms of Mesoscale Prussian Blue Analogue Particles in Modifier-free Synthesis. *Cryst. Growth Des.* **2020,** 20, 2713-2720.

(40) Felts, A.; Andrus, M.; Averback, C.; Li, C.; Talham, D., Comparison of the infrared absorptivities of some Prussian blue

analogues and their use to determine the composition of core-shell particles. *Polyhedron* **2017,** 133, 404-411.

(41) Abramoff, M.; Magalhaes, P.; Ram, S., Image processing with ImageJ. In ed.; Biophotonics International, 2004; Vol. 11.

(42) Felts, A.; Andrus, M.; Knowles, E.; Quintero, P.; Ahir, A.; Risset, O.; Li, C.; Maurin, I.; Halder, G.; Abboud, K.; Meisel, M.; Talham, D., Evidence for Interface-Induced Strain and Its Influence on Photomagnetism in Prussian Blue Analogue Core-Shell Heterostructures, $Rb_aCo_b[Fe(CN)_6]_c{\cdot}mH_2O@K_jNi_k[Cr(CN)_6]_l{\cdot}nH_2O$. *J. Phys. Chem. B* **2016,** 120, 5420-5429.

(43) Denton, A.; Ashcroft, N., Vegard Law. *Phys. Rev. A* **1991,** 43, 3161-3164.

(44) Scaramuzza, S.; Agnoli, S.; Amendola, V., Metastable alloy nanoparticles, metal-oxide nanocrescents and nanoshells generated by laser ablation in liquid solution: influence of the chemical environment on structure and composition. *Phys. Chem. Chem. Phys.* **2015,** 17, 28076-28087.

(45) Helm, L.; Merbach, A., Water exchange on metal ions: experiments and simulations. *Coord. Chem. Rev.* **1999,** 187, 151-181.

(46) Avendano, C.; Karadas, F.; Hilfiger, M.; Shatruk, M.; Dunbar, K., Cyanide Lability and Linkage Isomerism of Hexacyanochromate(III) Induced by the Co(II) Ion. *Inorg. Chem.* **2010,** 49, 583-594.

"For Table of Contents Use Only"

Design and synthesis of concentration gradient Prussian blue analogues.

SuKyung Jeon, Carissa H Li, and Daniel R. Talham*

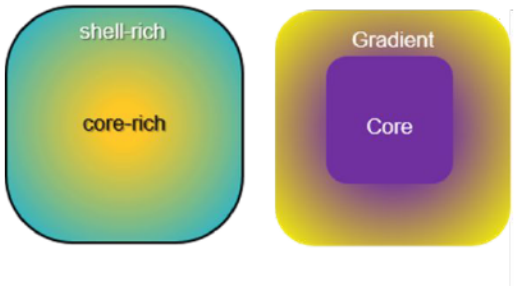

Mixed composition Prussian blue analogues (PBA) particles containing gradients in either the divalent metal or the hexacyanometallate components are prepared. The relative rate of precipitation of the PBA components is shown to be the crucial determinant for achieving control over the gradient synthesis, a parameter which is complicated by differing crystallization mechanisms within the PBA family.